

UNCLASSIFIED

Defense Technical Information Center
Compilation Part Notice

ADP013696

TITLE: Large Eddy Simulation of Transonic Turbulent Flow Over an Airfoil Using a Shock Capturing Scheme with Zonal Embedded Mesh

DISTRIBUTION: Approved for public release, distribution unlimited

This paper is part of the following report:

TITLE: DNS/LES Progress and Challenges. Proceedings of the Third AFOSR International Conference on DNS/LES

To order the complete compilation report, use: ADA412801

The component part is provided here to allow users access to individually authored sections of proceedings, annals, symposia, etc. However, the component should be considered within the context of the overall compilation report and not as a stand-alone technical report.

The following component part numbers comprise the compilation report:

ADP013620 thru ADP013707

UNCLASSIFIED

Best Available Copy

Best Available Copy

LARGE EDDY SIMULATION OF TRANSONIC TURBULENT FLOW OVER AN AIRFOIL USING A SHOCK CAPTURING SCHEME WITH ZONAL EMBEDDED MESH

ICHIRO NAKAMORI AND TOSHIAKI IKOHAGI

*Institute of Fluid Science
Tohoku University, Sendai, Japan*

Abstract

In this study, large eddy simulation(LES) of transonic flow around the NACA 0012 airfoil is performed accounting for the Leonard stress terms, the cross-stress terms and the subgrid-scale(SGS) Reynolds stress terms as the scale-similarity model at a free stream Mach number of 0.8, a Reynolds number of 9×10^6 and an angle of attack of 2.26° . An upwind finite volume formulation is used for the discretization of compressible spatial-filtered Navier-Stokes equations. To exclude excessive numerical damping due to the shock-capturing scheme, a hybrid method which uses linear combination of the third-order upwind scheme and the TVD scheme is employed. To reduce the total number of grid points, zonal embedded mesh is employed in the present LES analysis, in which a computational domain is decomposed near the wall-boundary. In the case represented here, it is shown that the statistical values in the turbulent boundary layer with shock/turbulence interaction is able to be estimated, and characteristics are clarified on the statistic of the turbulence.

1. Introduction

The analyses of unsteady flow on aircraft and fluid machinery in the transonic speed region will be required in future. With the recent development of the super-computer, LES will be used for such complicated flow field in future. Since the present LES analysis needs a shock-capturing scheme in the transonic region, it is required to investigate the effect of the inherent numerical dissipation on LES. Referring to third-order accurate shock-capturing scheme, the third order numerical viscosity is dominant in the smooth region, whereas the first-order viscosity is dominant in the region where the discontinuity appears. The numerical dissipation due to the third-order numerical viscosity is investigated by applying the fourth-order central scheme with the third-order numerical viscosity to the turbulent channel flow. As the results, the third-order viscosity with appropriate coefficient is found to be substituted in the Smagorinsky model on its SGS dissipation rate. Then, in this study, eddy viscosity SGS model is not used explicitly, and the third-order accurate scheme is used to substitute the SGS dissipation with the appropriate artificial viscosity coefficient. The analysis is carried out taking the sum of the Leonard stress terms, the cross-stress terms, and the SGS Reynolds stress terms as the scale-similarity model into account on the curvilinear coordinates. Still, the inviscid numerical flux is estimated by combining

the third-order scheme with the TVD scheme in order to stabilize the solution near the discontinuities.

A single structured grid is not suitable for LES at flight Reynolds numbers, since the viscous sublayer needs the very fine resolution in all directions(Chapman, 1979). As the result, the structured grid has numerous grid points throughout the domain. On the other hand, the unstructured grid is efficient to avoid the unnecessarily grid resolution for much of the computational domain(Jansen, 1999). The reduction of total number of grid points can be realized by the embedded mesh system. In this study, we have chosen the embedded mesh system to solve, because of the following points: 1) the number of grid points can be reduced in the spanwise and streamwise direction, 2) the computational efficiency is almost the same per unit cell in comparison with the efficiency in a single structured mesh system, and 3) it is comparatively effortless to improve the spatial accuracy.

2. LES Methodology

In this section, we summarize the LES methodology, including governing equations, SGS model, descretizing formula and numerical implementation.

2.1. GOVERNING EQUATIONS

The governing equations are the spatially filtered compressible Navier-Stokes equations. The spatial filtering removes the small-scale components of the fluid motion, retaining the unsteadiness associated with the large-scale turbulent motion. For an arbitrary function f , \bar{f} represents space-filtered variable. For compressible flows, it is expedient to define the Favre filtered variable \bar{f} . Applying these definitions to the compressible Navier-Stokes equations, we obtain the filtered governing equations

$$\frac{\partial \bar{\rho}}{\partial t} + \frac{\partial \bar{\rho} \bar{u}_i}{\partial x_i} = 0, \quad (1)$$

$$\frac{\partial \bar{\rho} \bar{u}_i}{\partial t} + \frac{\partial (\bar{\rho} \bar{u}_i \bar{u}_j + \delta_{ij} \bar{p} - \bar{\sigma}_{ij})}{\partial x_j} = - \frac{\partial \tau_{ij}}{x_j}, \quad (2)$$

$$\frac{\partial \bar{e}}{\partial t} + \frac{\partial (\bar{e} + \bar{p}) \bar{u}_j - \bar{\sigma}_{ij} \bar{u}_i - \kappa \frac{\partial \bar{T}}{\partial x_j}}{\partial x_j} = - \frac{\partial (q_j + d_j)}{x_j}, \quad (3)$$

$$\bar{p} = \bar{e} - \frac{\bar{\rho}}{2} \bar{u}^2 - \frac{\bar{\rho}}{2} \tau_{ii}, \quad (4)$$

where x_i represents the Cartesian coordinates($i=1, 2, 3$), $\bar{\rho}$ is the mean density, \bar{u}_i are the Cartesian components of the filtered velocity, \bar{p} is the mean pressure, τ_{ij} is the subgrid scale stress tensor, σ_{ij} is the molecular stress tensor, \bar{e} is the filtered total energy per unit volume, q_j is the subgrid heat flux, and d_j is the energy diffusion by the subgrid stresses. We neglect the summation term τ_{ii} in the equation of state, which would be very small compared to the thermodynamic pressure \bar{p} .

2.2. DESCRIPTORIZATION

The governing equations can be descretized in finite volume method for a control volume V with surface ∂V :

$$\frac{\partial}{\partial t} \int_V Q dV + \int_{\partial V} (E_1 n_{11} + E_2 n_{12} + E_3 n_{13}) dA = 0, \quad (5)$$

where

$$Q = \begin{bmatrix} \bar{\rho} \\ \bar{\rho}\tilde{u}_i \\ \bar{e} \end{bmatrix}, \quad E_i = \begin{bmatrix} \bar{\rho}\tilde{u}_i \\ \bar{\rho}\tilde{u}_i\tilde{u}_j + \delta_{ij}\bar{p} - \bar{\sigma}_{ij} + \tau_{ij} \\ \bar{\rho}\tilde{u}_i\bar{h}_i - \kappa \frac{\partial \bar{T}}{\partial x_i} - \bar{\sigma}_{ij}\tilde{u}_i + q_i + d_i \end{bmatrix}. \quad (6)$$

$(n_{11}, n_{12}, n_{13})^t$ denotes the normal vector to each cell-interface. The explicit Runge Kutta method is employed for the time integration. The third-order numerical inviscid flux $f_{i+1/2}^{(3rd)}$ is estimated by using the fourth-order central scheme and the additional third-order dissipation.

$$f_{i+1/2}^{(3rd)} = f_{i+1/2}^{(4th)} + \varepsilon_4(R|\Lambda|)_{i+1/2}(\alpha_{i+3/2} - 2\alpha_{i+1/2} + \alpha_{i-1/2}), \quad (7)$$

$$f_{i+1/2}^{(4th)} = f_{i+1/2}^{(4th)}(Q_{i+1/2}^L, Q_{i+1/2}^R), \quad (8)$$

$$\alpha_{i+1/2} = R_{i+1/2}^{-1} \Delta_{i+1/2} Q, \quad (9)$$

where R and Λ represent the diagonalization matrix of the right eigenvectors and the diagonal matrix of the eigenvalues, respectively. The values of each variables on either side of cell interfaces are

$$\begin{aligned} Q_{i+1/2}^L &= Q_i + \frac{1}{12}(\Delta_{i-1/2}Q + 6\Delta_{i+1/2}Q - \Delta_{i+3/2}Q), \\ Q_{i-1/2}^R &= Q_i - \frac{1}{12}(\Delta_{i+1/2}Q + 6\Delta_{i-1/2}Q - \Delta_{i-3/2}Q). \end{aligned} \quad (10)$$

The values of artificial viscosity coefficient ε_4 is calibrated at 1/256 in the airfoil simulation.

The method mentioned above cannot treat the transonic flow, since the shock wave appears. Then, the numerical flux $f_{i+1/2}^{TVD}$ is differently prepared by using a finite difference splitting(Roe, 1981) and extrapolated variables $\bar{Q}_{i\pm 1/2}^{R/L}$ with a slope-limiter(Daiguji *et al.*, 1997). To exclude excessive numerical damping due to the limiter, we employ self-adjusting hybrid, that uses linear combination of the third-order upwind scheme and the TVD scheme. the numerical flux $f_{i+1/2}$ is blended as follows:

$$f_{i+1/2} = (1 - \theta)f_{i+1/2}^{(3rd)} + \theta f_{i+1/2}^{TVD}, \quad (11)$$

$$\theta = \begin{cases} 0, & \text{for } \frac{|\bar{\rho}_{i+1} - 2\bar{\rho}_i + \bar{\rho}_{i-1}|}{\bar{\rho}_{i+1} + 2\bar{\rho}_i + \bar{\rho}_{i-1}} \leq 0.01 \\ 1, & \text{for } \frac{|\bar{\rho}_{i+1} - 2\bar{\rho}_i + \bar{\rho}_{i-1}|}{\bar{\rho}_{i+1} + 2\bar{\rho}_i + \bar{\rho}_{i-1}} > 0.01 \end{cases}. \quad (12)$$

2.3. SGS MODEL

SGS stresses can be decomposed into the following terms(Leonard, 1974):

$$\tau_{ij} = L_{ij} + C_{ij} + R_{ij}, \quad (13)$$

the Leonard stress terms, $L_{ij} = \bar{\rho}(\tilde{u}_i\tilde{u}_j - \bar{u}_i\bar{u}_j)$; the cross-stress terms, $C_{ij} = \bar{\rho}(\tilde{u}_i\tilde{u}'_j + \tilde{u}'_i\tilde{u}_j)$; and the SGS Reynolds stress terms, $R_{ij} = \bar{\rho}\tilde{u}'_i\tilde{u}'_j$. Present study follows the hypothesis that

the SGS energy dissipation would be substituted in the numerical dissipation due to the inherent artificial viscosity of the shock-capturing scheme. Consequently, the eddy viscosity model was not employed in the present LES analyses. However, a scale-similarity model is taken into account. They can be estimated using Taylor expansion. To eliminate the terms which violate the Galilean invariance(Speziale, 1985), these terms are summated with the Bardina model(Bardina *et al.*, 1980) being applied to the cross-stress terms and the SGS Reynolds stress terms.

$$\begin{aligned} L_{ij} + C_{ij} + R_{ij} &\approx \bar{\rho}(\tilde{u}_i \tilde{u}_j - \tilde{u}_i \tilde{u}_j) \\ &= \frac{\bar{\rho}}{12} \Delta_k^2 \frac{\partial \tilde{u}_i}{\partial x_k} \frac{\partial \tilde{u}_j}{\partial x_k} + O(\Delta_k^4) \end{aligned} \quad (14)$$

For the SGS terms q_j and d_j in energy equation, the following models are employed by approximating $u_j \cong \tilde{u}_j$ and $T \cong \tilde{T}$.

$$\begin{aligned} q_j &= C_p \bar{\rho}(\tilde{u}_j \tilde{T} - \tilde{u}_j \tilde{T}) \cong C_p \bar{\rho}(\tilde{u}_j \tilde{T} - \tilde{u}_j \tilde{T}) \\ &= \frac{C_p}{12} \Delta_k^2 \frac{\partial \tilde{T}}{\partial x_k} \frac{\partial \tilde{u}_j}{\partial x_k} + O(\Delta_k^4), \end{aligned} \quad (15)$$

$$\begin{aligned} d_j &= \frac{1}{2} \bar{\rho}(\tilde{u}^2 \tilde{u}_j - \tilde{u}^2 \tilde{u}_j) \\ &\cong \frac{\bar{\rho}}{24} \Delta_k^2 \frac{\partial \tilde{u}_i}{\partial x_k} \frac{\partial \tilde{u}_i}{\partial x_k} \tilde{u}_j + \frac{\bar{\rho}}{24} \Delta_k^2 \frac{\partial \tilde{u}^2}{\partial x_k} \frac{\partial \tilde{u}_j}{\partial x_k} + O(\Delta_k^4), \end{aligned} \quad (16)$$

where a perfect gas with a constant specific heat capacity C_p is assumed.

3. Results and Discussion

3.1. CODE VALIDATION

A validation test for the shock-capturing is performed for the shock tube problem(Shu *et al.*, 1989), which has several extrema in the smooth region. Figure 1 shows the solution via the present method with 400 cells. For the comparison, we have included the line of solution via the 8th-order ENO scheme(Harten, 1989) with 1600 cells. Note that there is no serious overshooting or undershooting neat the discontinuity. This fact shows that the present method is suitable for LES with strong discontinuities.

A validation test for large eddy simulation is carried out by applying the present method to the channel flow. The analyses are performed for the turbulent plane Couette flow of $8.0h \times 2.0h \times 4.0h$ at $Re(\frac{\rho_w U_{wh}}{\mu_w}) = 1300$ and the Mach number $M(\frac{U_w}{c_w}) = 0.3$. The number of cells is (64,64,32) with the size of cells in the wall coordinate varying from 1 to 1.4 wall units. Figure 2 shows the mean velocity profiles via the TVD scheme and the present method. The ensemble data are obtained from the averaged flow over 100000 time steps. We have included incompressible DNS results(Bech *et al.*, 1995) for the comparison. The artificial coefficient ϵ_4 is calibrated at 1/256, that is also used in the present airfoil simulation. In this case, the hybridization of the scheme is absolutely necessary since the inherent numerical dissipation due to the flux-limiter of the TVD-scheme becomes dominant.

In Fig. 3 we show the mean velocity profiles with and without the SGS models for the same channel flow. We have included the root mean square (*rms*) of the velocity

components in Fig. 4. The predictions in all *rms* quantities, especially the streamwise component, are of great improvement by using the present SGS models, although a little bit greater artificial coefficient ε_4 of 1/128 is taken to produce more dissipative solution compared to the DNS results.

3.2. AIRFOIL SIMULATION

The flow configuration is that of experiments(Harris, 1981) at a Reynolds number based on chord $Re = 9 \times 10^6$, a free-stream Mach number $M = 0.8$, and an angle of attack $\alpha = 2.26^\circ$. A single structured grid system makes it difficult to perform LES for the flow of the present Reynolds number. The use of embedded mesh reduces the computational memory and the CPU to some extent. The mesh size is refined near the wall and the mesh system is replaced 6 times toward the wall surface regarding the streamwise direction and the spanwise direction so that the large eddy can be resolved, as shown in Fig. 5. The extent of spanwise direction is chosen as $L_z = 0.04c$. Current simulation employs approximately 11 million cells.

Figure 6 shows the instantaneous Mach number distribution in the mid-span plane. On the suction side, the shock wave appears at about 60% of the chord length from the leading edge. It is found that there is no serious numerical oscillation near the shock wave. Figure 7 shows the isosurfaces of instantaneous spanwise velocity \tilde{w} on the suction side. Weak three-dimensionalization occurs, and secondary flow is formed(Fig. 8). It is also shown that the three-dimensionalized structure becomes larger, as it goes to the trailing edge, as shown in Fig. 9. The increase of the friction coefficient can be also confirmed with the relation to the three-dimensionalization. In Fig. 10, we show the friction coefficient, which increases at about 5% of the chord length from the leading edge on the suction side where the transition takes place naturally.

Figure 11 shows mean wall pressure distribution, which almost agrees with the experimental result, however there is a little discrepancy of the shock position between the simulation and the experimental data. The aspect of the pressure distribution under the influence of adverse pressure gradient by the shock wave is predicted so as to produce the B. L. separation more extensively.

Figures 12 and Fig. 13 show the turbulence energy profiles on the pressure side and the suction side, respectively. The distance from the wall is represented by η . On the suction side, the turbulence energy rises ($x/c = 0.7$) behind the shock wave, while it contrastively decreases downstream the position of ($x/c = 0.4$) on the pressure side.

The spanwise one-dimensional energy spectrum distribution is examined in order to understand whether it reproduces the energy cascade process in the turbulent boundary layer. The energy spectrum is defined as,

$$E_{i,i}(k) = \frac{2}{\pi} \int_0^\infty R_{i,i}(r) e^{-ikr} dr, \quad (17)$$

where $R_{i,i}$ represents the correlation tensor given by

$$R_{i,i}(r) = \langle u'_i(x) u'_i(x+r) \rangle. \quad (18)$$

u'_i is approximated by using the grid-scale differences $\tilde{u}_i - \langle \tilde{u}_i \rangle$. r is in spanwise direction in this case. Figure 14 shows the spanwise one-dimensional energy spectra of the velocity at $y^+ \cong 10$. It is confirmed that the energy cascade with the close gradient of the 5/3 law in the sampling point ($x/c = 0.4, 0.7$) is obtained.

4. Conclusions

The scale-similarity models are taken into account in the generalized curvilinear coordinate system in order to represent the SGS effect which includes the backscatter in the energy cascade in turbulent boundary layer. To keep the resolution of the near wall turbulence, the embedded mesh system is employed in this study. Also, an highly accurate scheme is obtained in order to capture generation of the turbulent boundary layer from the leading edge and its developing process. Concurrently, the present hybridization of the scheme produces no serious oscillation near the shock wave in the present simulation. As a result of applying the present method to transonic turbulent flow around the airfoil, it is possible to reproduce the flow field with large-scale structure of the turbulent boundary layer. It is found that the qualitative analysis is possible on the turbulent characteristics, that includes the interaction with shock wave by the present LES method.

5. Acknowledgement

The simulations were performed using the super-computer, SX-5 in the Institute of Fluid Science, Tohoku University.

References

- Bardina, J., Ferziger, J. H. and Reynolds, W. C. (1980) Improved subgrid scale models for large eddy simulation. *AIAA Paper 80-1357*
- Bech, K., Tillmark, H., Alfredsson, N. and Andersson, H. I. (1995) Investigation of turbulent plane Couette flow at low Reynolds number. *J. Fluid Mech.* **286**, pp. 291-325
- Boris, J. P., Grinstein, F. F., Oran, E. S. and Kolbe, R. L. (1992) New insights into large eddy simulation. *Fluid Dynam. Res.* **10**, pp. 199-228
- Chapman, D. R. (1979) Computational aerodynamics development and outlook. *AIAA J.* **17**, pp. 1293-1313
- Clark, R. A., Ferziger, J. H. and Reynolds, W. C. (1979) Evaluation of subgrid-scale models using an accurately simulated turbulent flow. *J. Fluid Mech.* **91**, pp. 1-16
- Daiguji, H., Yuan, X. and Yamamoto, S. (1997) Stabilization of higher-order high resolution schemes for the compressible Navier-Stokes equations. *Numer. Meth. Heat. & Fluid Flow* **7**, pp. 250-274
- Garnier, E., Mossi, M., Sagaut, P., Comte, P. and Deville, M. (1999) On the use of shock-capturing schemes for large-eddy simulation. *J. Comp. Phys.* **153**, pp. 273-311
- Harris, C. D. (1981) Two-dimensional aerodynamic characteristics of the NACA 0012 airfoil in the Langley 8-foot transonic pressure tunnel. NASA TM 81927
- Harten, A. (1989) ENO schemes with subcell resolution. *J. Comp. Phys.* **83**, pp. 148-184
- Jansen, K. E. (1999) A stabilized finite element method for computing turbulence. *Comp. Meth. in Appl. Mech. and Eng.* **174**, pp. 299-317
- Leonard, A. (1974) On the energy cascade in large eddy simulations of turbulent fluid flows. *Adv. Geophys.* **18A**, pp. 237-248
- Moin, P. and Jimenez, J. (1993) Large eddy simulations of complex turbulent flows. *AIAA Paper-93-3099*
- Roe, P. L. (1981) Approximate Riemann solvers, parameter vectors and difference schemes. *J. Comp. Phys.* **43**, pp. 357-372
- Shu, C-W. and Osher, S. (1989) Efficient implementation of essentially non-oscillatory shock-capturing schemes. *J. Comp. Phys.* **83**, pp. 32-78
- Speziale, C. G. (1985) Galilean invariance of subgrid-scale stress models in the large eddy simulation of turbulence. *J. Fluid Mech.* **156**, pp. 55-62

Best Available Copy

Best Available Copy

LARGE EDDY SIMULATION OF TRANSONIC TURBULENT FLOW

749

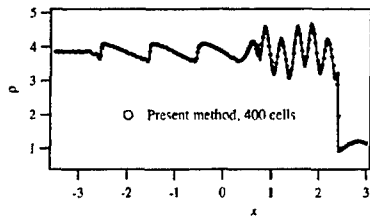


Figure 1. Code verification for the shock-capturing

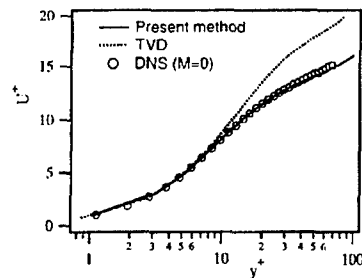


Figure 2. Code verification for the channel turbulent flow

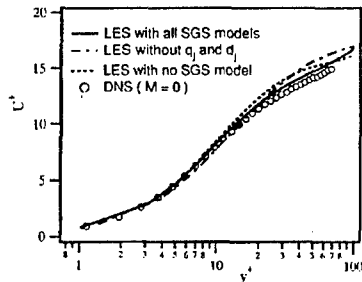


Figure 3. Model verification for the channel turbulent flow

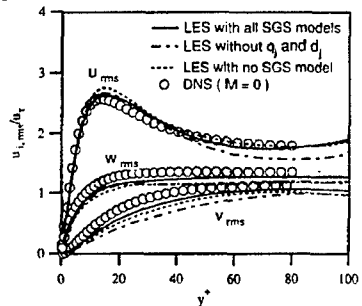


Figure 4. Model verification for the channel turbulent flow

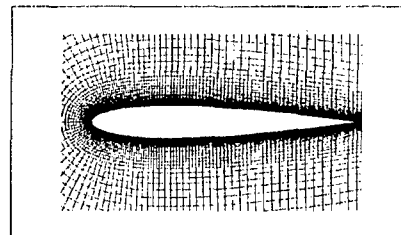


Figure 5. Side view of embedded mesh around the NACA0012 airfoil

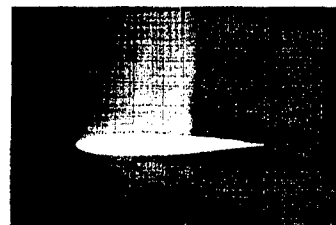


Figure 6. Side view of instantaneous Mach number contours

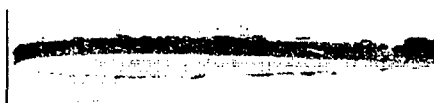


Figure 7. Isosurfaces of spanwise velocity

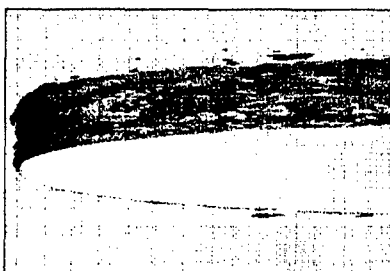


Figure 8. Isosurfaces of spanwise velocity near the leading edge

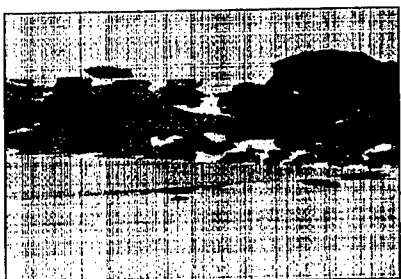


Figure 9. Isosurfaces of spanwise velocity near the trailing edge

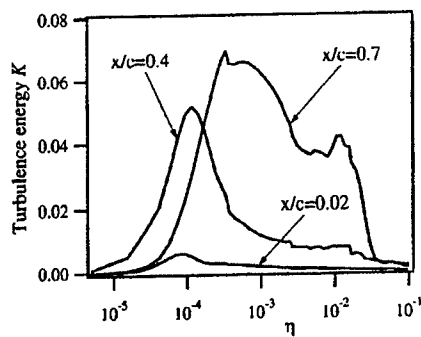


Figure 12. Turbulence energy profiles on the suction side

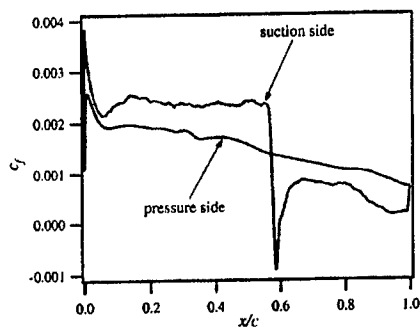


Figure 10. Skin friction distribution

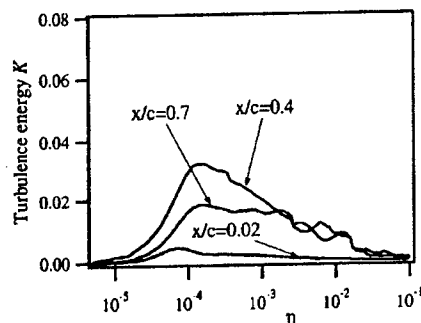


Figure 13. Turbulence energy profiles on the pressure side

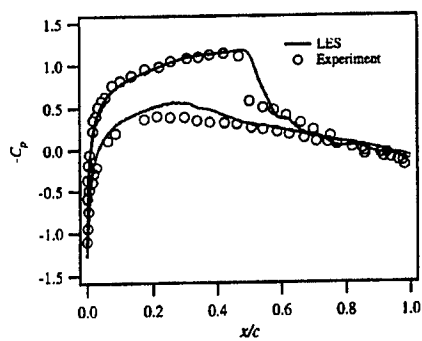


Figure 11. Wall pressure distribution

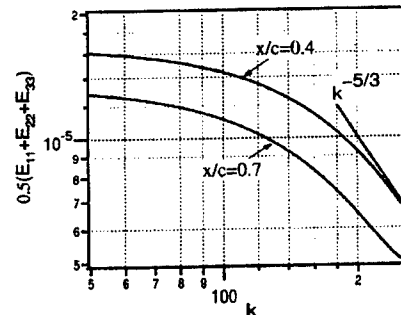


Figure 14. Spanwise one dimensional energy spectra on the pressure side at $y^+ \approx 10$

Best Available Copy